Solar Physics (2004) 225: 379–401

OBSERVATIONS OF CME-RELATED PHENOMENA IN A WIDE SPECTRAL RANGE

V. V. GRECHNEV[1], V. G. ZANDANOV[1], A. M. URALOV[1], V. P. MAKSIMOV[1]
V. G. RUDENKO[1], V. N. BOROVIK[2], G. B. GELFREIKH[2], I. Y. GRIGORIEVA[2],
V. G. MEDAR[2] and A. N. KORZHAVIN[3]
[1]*Institute of Solar-Terrestrial Physics, P.O. Box 4026, Lermontov Street 126, Irkutsk 664033, Russia*
(e-mail: grechnev@iszf.irk.ru)
[2]*Main (Pulkovo) Astronomical Observatory of RAS, St. Petersburg, Russia*
[3]*Special Astrophysical Observatory, St. Petersburg's Branch, St. Petersburg, Russia*

(Received 26 February 2004; accepted 19 September 2004)

Abstract. We study pre-eruptive, eruptive, and post-eruptive phenomena related to a CME that occurred on November 23, 2000 by means of joint analyses of data from various spectral ranges. Almost all known CME-associated phenomena were observed during this event, i.e., a filament eruption, solar flare, dimmings, and a post-eruptive arcade formation. Following a chain of events observed in various spectral ranges, we find that the event occurred in an activity complex consisting of active regions 9231 and 9238, and that it was triggered by a magnetic flux emergence, which caused a flare in AR 9231. In turn, the flare triggered activation and eruption of the filament followed by the CME and the flare in AR 9238 in which the post-eruptive arcade was observed. We discuss some characteristics of the flare and CME and also estimate the magnetic field strength in the coronal arcade to be about 200 G from spatially resolved polarization measurements in microwaves with radio telescopes. In this particular case, the only significant emission mechanism is optically thin free-free emission, and the possible contribution of nonthermal emissions cannot change our estimate of the magnetic field strength in the corona. However, generally one should make sure that the nonthermal contribution cannot be important in similar cases; otherwise, the magnetic field can be well overestimated. Here, we specifically address the identification technique of the radio emission mechanism.

1. Introduction

Coronal mass ejections (CMEs) are considered to be the major cause of powerful geomagnetic disturbances. Therefore, studies of CMEs at various stages of their development are important, especially at the initiation stage, when they can be followed, in principle, in observations on the solar disk. CMEs are accompanied by other manifestations of solar activity, i.e., eruptive filaments/prominences, solar flares, temporary depressions – dimmings (transient coronal holes), coronal and chromospheric waves, and post-eruptive arcade formation at the site of the pre-existing filament/prominence. Interrelation of these phenomena is still far from the comprehensive understanding; CME trigger mechanisms are not clear. To make progress in the solution of the problems, joint studies of these complex phenomena in a wide spectral range as well as estimates of physical conditions of the relevant processes are necessary.

In the 1990s, causal relations between solar flares, eruptive prominences, and CMEs were extensively discussed. The discussion inspired by Gosling (1993) revealed contradictory opinions about the nature of the connections between those phenomena. The major problem of the interpretation was the absence of observations of CMEs against the background of the solar disk, so there was no way to follow the whole chain of events.

Several instruments that appeared in the 1990s significantly enhanced the opportunities to study eruptive and post-eruptive phenomena. Spaceborne observations on *Yohkoh*, SOHO, and TRACE spacecraft, two-dimensional imaging observations at the Nobeyama Radioheliograph (NoRH, 17 GHz) and the Siberian Solar Radio Telescope (SSRT, 5.7 GHz), high spectral resolution one-dimensional observations at the RATAN-600 (1–17 GHz) contribute essentially to the experimental material. However, there is no impressive progress in solving the problems listed, and the questions mentioned above remain unsolved. There are two reasons for this. Solar eruptive phenomena are complex; hence, to understand their nature, joint analysis is necessary of data available in various spectral ranges of the solar emission. On the other hand, this requires processing and analysis of large amounts of observational data, which presents methodical difficulties.

In this paper, we study pre-eruptive, eruptive, and post-eruptive phenomena associated with a CME of November 23, 2000. Almost all possible CME-related phenomena were observed against the background of the solar disk during this event. We investigate this event by means of joint analysis of data obtained in extreme ultraviolet (SOHO/EIT), soft X-rays (*Yohkoh*/SXT and GOES), microwaves at 17 GHz (NoRH) and 5.7 GHz (SSRT), multifrequency radio data from RATAN-600, Hα filtergrams (Yunnan Observatory), SOHO/MDI magnetograms, and SOHO/LASCO images of the corona. Such a comprehensive study of a particular event makes possible understanding its whole story and estimating physical parameters in the region of the event. On the other hand, we endeavor to contribute material for further statistical studies of CME-related phenomena.

Multispectral observations of phenomena accompanying the eruption as well as before and after it are considered in Section 2 where some data analysis techniques are also addressed. The observational data are discussed and interpreted in Section 3. In particular, the overall story of the event, plasma diagnostics, and magnetic field estimation are addressed there. The major conclusions are given in Section 4.

2. Observations

2.1. The situation before the eruptive event

Two active regions were observed on November 23, 2000 in the southwest quadrant of the solar disk. They are 9231 (W55 S25) whose magnetic configuration was complex, and 9238 (W40 S26), which had almost decayed. Photospheric magnetograms produced by SOHO/MDI with an interval of 96 min allow one to follow changes that occurred during 48 h from November 22 through 23. Figure 1 shows a difference image produced by the subtraction of two magnetograms separated by 3 h (a); two magnetograms separated by 24 h to demonstrate the overall reconstruction of the magnetic fields (b, c); and a variance image (Grechnev, 2003) showing the variability of each pixel in the set of 29 magnetograms produced within those 48 h (d). Labels 1 and 2 mark two regions of the most important transformations where the magnetic field strength variations exceed 350 G in 96 min. In summary, Figure 1 shows appreciable changes that occurred in the magnetic structure during 22 through 23 November, in particular, intrusion of an S-polarity region (black in the figure) into pre-existing N-polarity patch 2 that indicates emergence of a new bipolar magnetic flux 1–2.

A horseshoe-shaped filament well visible in Hα was located northward of those regions. The curve of this filament was directed northward, and its ends were bent toward regions 9238 and 9231 (Figure 2; no Hα images are available in between of 05:12 and 05:47 UT). Some hours before the CME, the filament was activated and lengthened. Its southeast end intruded into region 9238 along the magnetic neutral line, and its southwest end reached region 9231.

On November 23, some activities took place in both active regions, especially in AR 9231, being manifest in extreme UV (SOHO/EIT, 195 Å) and other spectral ranges. For example, subflares were observed in AR 9231 during 02:34 – 02:52 and 04:09 – 04:16 (time hereafter is UT). Some episodes of a subflare are shown by the difference Hα images in Figure 3. Propagation of brightenings along the axis of the sunspot group 9231 toward the filament (indicated by the arrows) can be also seen. This motion is quite well visible in the movie mode.

2.2. The eruptive event

The eruptive event of November 23, 2000 occurred in AR 9238 (W40 S26). The event starts with disappearance of the filament in Hα between 05:12 and 05:47 (see Figure 2) and brightening of coronal loops visible in the SOHO/EIT 195 Å image of 05:36. Ejection of the filament likely occurs, which is confirmed by the SOHO/EIT images of 05:48 and 06:00. This can be seen from Figure 4 where several SOHO/EIT 195 Å images are shown. The images in the left column are shown nonlinearly to display simultaneously bright and dark features. The three right columns show difference images produced by subtraction of the same frame of 05:00. The they differ by the range of brightness to reveal various features of the event. The brightness of the images in the second column from left is not limited. The brightness range in the third column is ± 500 (instrumental counts per pixel), and in the right column it is ± 50 (the maximum brightness is about 7000 at 06:00).

Two frames of 05:48 and 06:00 in the right column show a bright extended feature, emitting material associated with the eruptive filament. The second column

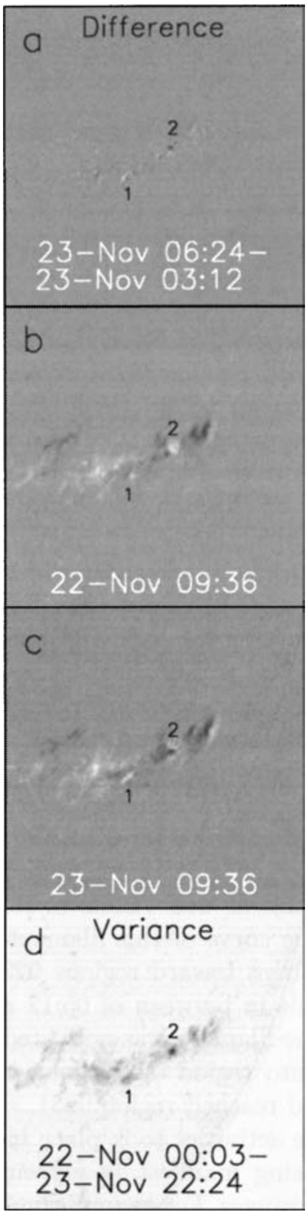

Figure 1. SOHO/MDI magnetograms of active regions 9231 and 9238. a) Difference of the magnetograms observed on November 23 at 06:24 and at 03:12. b) and c) Two magnetograms separated by day and night, and well before and after the event. d) Variance image composed from all 29 magnetograms observed during 2 days.

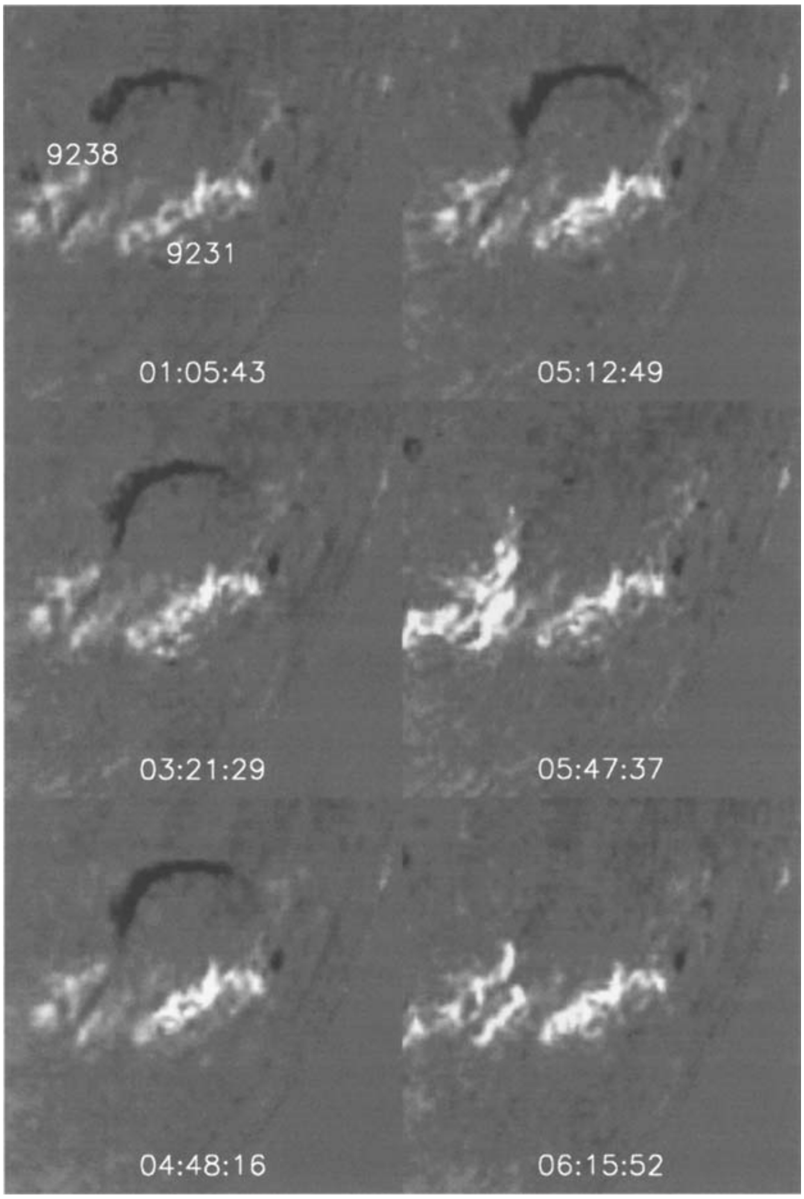

Figure 2. Hα images of the event obtained at the Yunnan Observatory. Limb darkening is compensated.

shows brightening of coronal structures. It occurs at 05:36 in AR 9238, and still earlier in AR 9231.

A flare of 1F /C5.4 importance occurs during 05:36–06:15 with a maximum at 05:48. Flare ribbons are well visible in the Hα line, and flaring coronal loops are conspicuous in extreme UV (SOHO/EIT) and soft X-ray (*Yohkoh*/SXT) emissions.

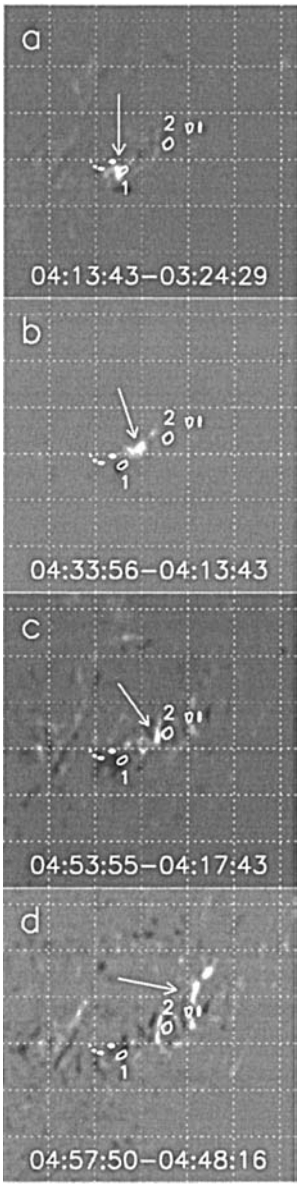

Figure 3. Hα subflare preceding the event. All panels show difference images to reveal brightenings (pointed out by the *arrows*). Labels 1 and 2 show the same spatial positions as in Figure 1.

Other manifestations of the event are as follows. A powerful type III burst in the band of 40–1100 MHz with a total flux of about 350 s.f.u. at 500 MHz was recorded at the Culgoora and Hiraiso observatories during 05:36–05:40. A weak burst of 11 s.f.u. (maximum brightness temperature of 0.1 MK at 17 GHz) was observed in microwaves with the NoRH at 17 GHz and the SSRT at 5.7 GHz from 05:35 on

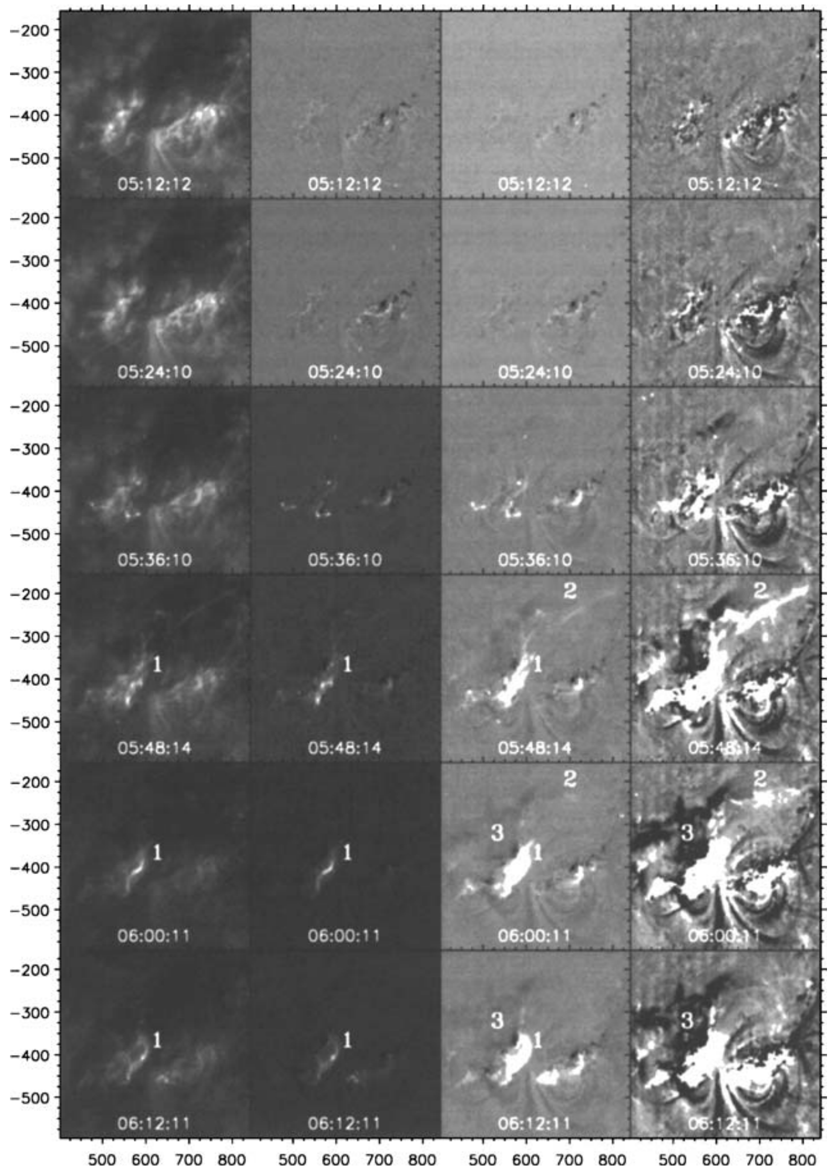

Figure 4. Images observed with SOHO/EIT, 195 Å. All columns show the same times, but in different representation. Three right columns show difference images. Nonlinear brightness scaling is applied to show simultaneously the arcade (1), ejecta (2), and dimming (3). Axes show arc seconds from the solar disk center.

with a maximum at 05:55. Since the emitting sources at 17 GHz are rather weak, especially before the event, we constructed NoRH images with long integration times of 10 and 120 s (in contrast to 1 s in the standard snapshot mode) to enhance the sensitivity.

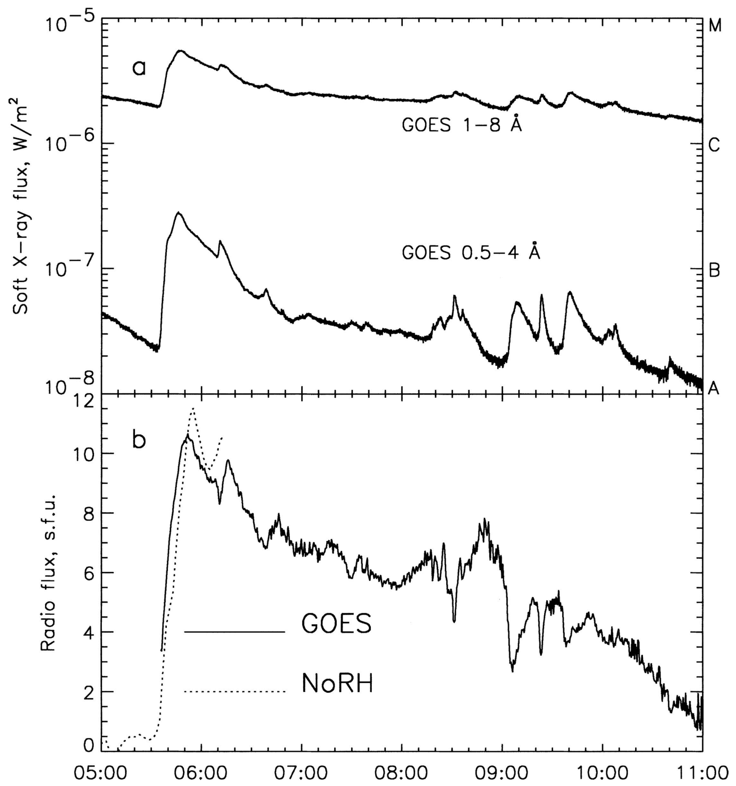

Figure 5. Time profiles of the microwave and soft X-rays bursts. *Top*: GOES-8 data. *Bottom*: radio flux measured from images produced with NoRH at 17 GHz and the total radio flux of thermal bremsstrahlung estimated from GOES-8 data.

The time profile of the initial part of the flare microwave emission observed with NoRH at 17 GHz is plotted in Figure 5 along with radio flux of the optically thin thermal bremsstrahlung estimated from soft X-ray GOES data for the entire interval of our analysis. The total radio flux is computed from two-dimensional NoRH radio maps as $S_{[\mathrm{sfu}]} \approx 7.22 \times 10^{-11} \nu^2_{[\mathrm{GHz})} \rho^2{}_{[\mathrm{arcsec}]} \sum_i T_{\mathrm{B}i[\mathrm{K}]}$, where $T_{\mathrm{B}i}$ is the brightness temperature of a pixel (with a width ρ). The thermal radio flux is computed from soft X-ray data as $S_{[\mathrm{sfu}]} \approx 3 \times 10^{-45} EM_{[\mathrm{cm}^{-3}]} T^{-1/2}_{[\mathrm{K}]}$. The emission measure *EM* and temperature *T* of the emitting plasma are computed from GOES data using the GOES software by R. Schwartz. A great deal of similarity of the observed and estimated light curves is seen.

The images of the flare region obtained with the SSRT and NoRH resemble each other. The flare configuration in microwaves is complex, with several alternately brightening, moving sources (Figure 6). Sources 4 and 5 appear before the flare, at 04:50 – 05:15, and then they brighten again. Sources 1 and 3 brighten almost simultaneously, and the appearance of sources 6 and 7 is somewhat delayed. Source 2 appears after all others, being related to the secondary peak of 06:15.

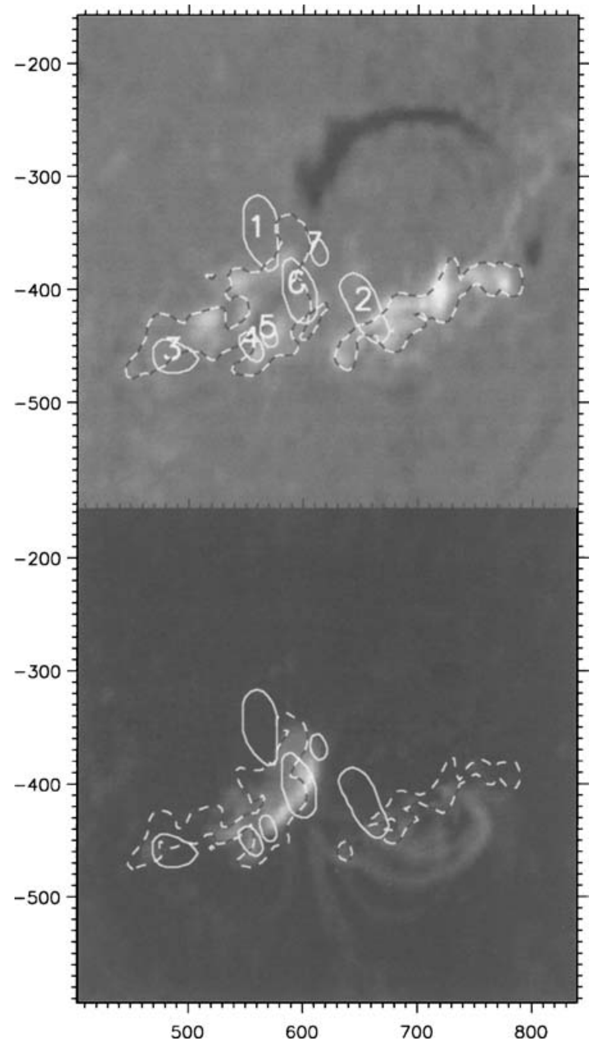

Figure 6. Structures observed in different spectral ranges during the flare event in the chromosphere and the corona. *Top*: structures observed in Hα (halftone, 05:13) and at 17 Ghz. *Bottom*: relative disposition of bright regions in the chromosphere and corona. Halftone background shows a difference EUV image produced by subtraction of SOHO/EIT 195 Å frames at 06:36 and 05:00. Lower panel show coronal loops connecting both active regions, 9238 and 9231. Black/white contours in both panels show flare ribbons observed in Hα at 05:47. White oval contours in both panels show active microwave sources detected during the flare. Axes show arc seconds from the solar disk center.

The brightest source 6 coincides with the arcade observed in EUV and soft X-ray emissions. The source is weakly polarized with a degree varying in the course of the flare (Figures 7 and 8). Figure 7 shows two microwave images observed at 17 GHz at 05:45 and 06:05 as a halftone background along with the magnetogram and Stokes *V* data shown as contours. The same SOHO/MDI magnetogram observed

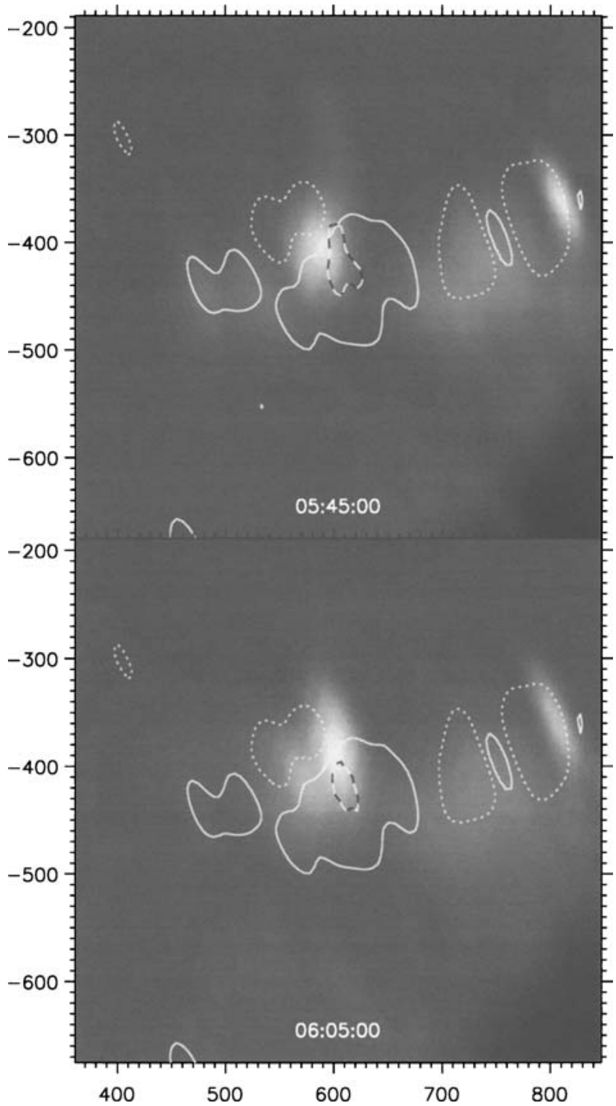

Figure 7. Radio images at 17 Ghz (grayscale – Stokes *I*, dashed black/white contours – Stokes *V*) overlaid with white contours of the magnetogram at 04:48 UT convolved with NoRH beam pattern, same for both panels (*solid – N*, *dotted – S*, levels are the same by the absolute value). Axes show arc seconds from the solar disk center. Note the displacement of the total intensity source along the magnetic neutral line.

at 04:48 is shown as white contours (solid – *N*, dotted – *S*). To fit radio observations, we convolved the magnetogram with the NoRH beam pattern. The maximum magnetic field strength (−420, 840) G is reached in compact features visible in the initial magnetogram, and the maximum strength is (−60, 200) G in the convolved

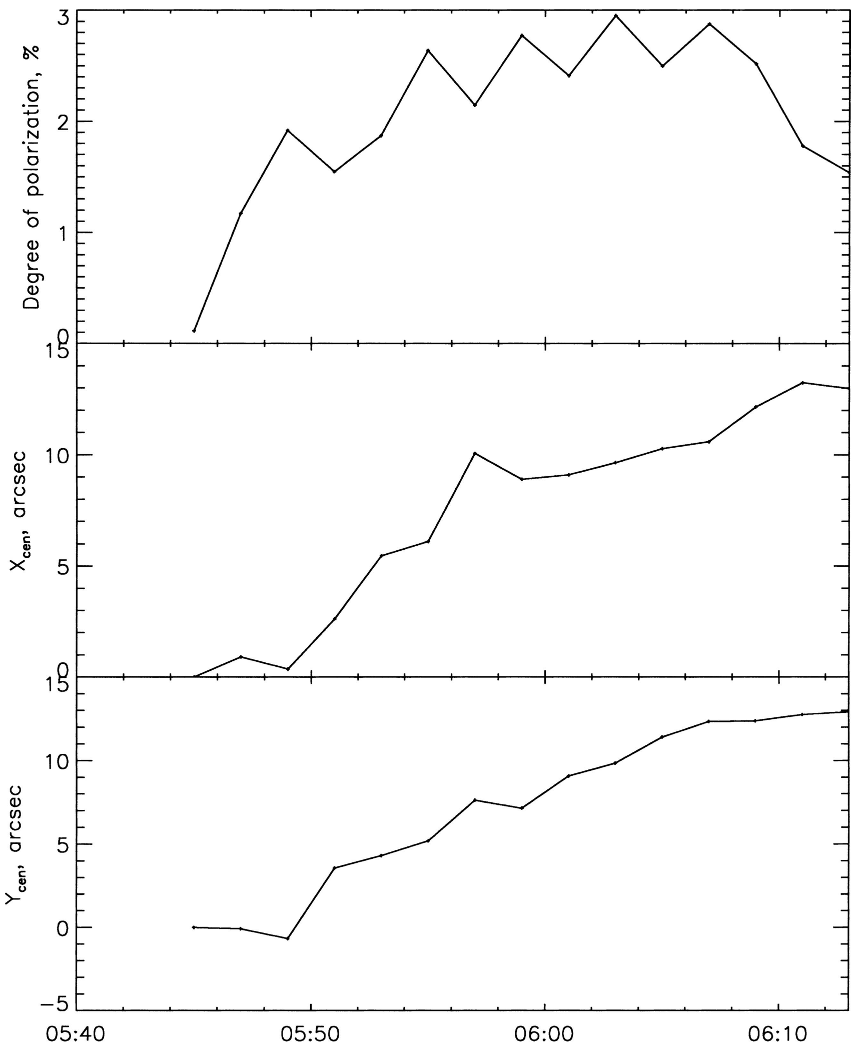

Figure 8. Top: variations of the degree of polarization at 17 GHz (mean over the polarized region), *middle* and *bottom*: coordinates of the brightness center of the total intensity source.

magnetogram. Taking into account that the contour levels in Figure 7 are the same absolute value (±25 G), we see that the microwave source in total intensity is close to the magnetic neutral line and moves along it (see the coordinates of the brightness center shown in Figure 8).

The microwave source observed in total intensity is strongly displaced with respect to the maximum of the polarized emission. Hence, the distribution of the degree of polarization over the microwave source is not uniform, with a strong slope southwestward, both at 17 and 5.7 GHz. The degree of polarization in the region of the 17 GHz source is 5–7% before the event, while at the onset of the flare it drops almost to zero, and then increases again up to 3%. Its variations in the course of the flare are shown in Figure 8. The upper panel in this figure shows the mean degree of polarization averaged over the polarized region. The degree of polarization in this region, measured at 5.7 GHz within the interval of 06:06 – 06:12, is 7–8%. These facts suggest that we observe an arcade with its top part above the magnetic neutral line being unpolarized, and the polarized emission escaping from legs of loops constituting the arcade.

Figure 6 shows the correspondence of the structures observed in Hα, EUV, and at 17 GHz. The active radio sources were revealed using the variance method (Grechnev, 2003). The halftone background shows the last Hα frame prior to the event, at 05:12:49. White contours show active radio sources that appeared during the event, and broken contours show bright regions in Hα in the first frame after the eruption, 05:47:37. No Hα image in between these two is available. The lower panel shows a difference SOHO/EIT 195 Å image produced by subtraction of two frames, at 06:36 and 05:00. The figure shows relative disposition of bright chromospheric regions observed in Hα and bright coronal features observed in EUV and microwaves.

From 06:06 on, SOHO/LASCO observed a CME propagating with a speed of 500 – 600 km s^{-1} within position angles of about 215°, which corresponds to the position of the event site within the southwest quadrant of the solar disk. The CME launch time estimated using the extrapolated time-height plot inferred from the LASCO data is in accord with the onset time of the eruptive event in the chromosphere and the lower corona.

2.3. Post-eruptive phenomena

The flare is followed by a series of subflares in AR9231 during 06:11– 06:19, 08:26 –8:42, 09:23– 09:29, 09:38– 09:44, 10:06 –10:13, and weak brightenings in AR 9238. The subflares are also detectable in extreme ultraviolet (SOHO/EIT) and in soft X-rays (*Yohkoh*/SXT). This slender activity is also detectable in GOES light curves (see Figure 5). A post-eruptive arcade at the site of the eruption is observed in those spectral ranges for a long time, up to at least 11 UT. The emission of the arcade is recorded with the RATAN-600 in the whole range of the instrument of 1.7–30 cm in three azimuths, i.e., at 07:52, 09:00, and 10:08. The arcade is manifest as a wide, bright radio source identified with the region on the solar disk where the ejection of the filament and subsequent flare are observed (Borovik *et al.*, 2002a,b). The RATAN-600 records show that the total flux spectrum in the range of 1.8–10 cm is flat (with an accuracy of 20%), and the size of the source is constant at all frequencies where it could be measured. These result in a brightness temperature spectrum of $T_{\mathrm{B}} \sim \lambda^2$. Note that the radio observations at 1.76 cm with NoRH at 06 UT agree well with the observations with RATAN-600 at 08 –10 UT in spatial structure, flux density, and polarization.

Other post-eruptive features, dimmings, are detectable in three lower frames in Figure 4 as dark regions in northeast quadrant and extreme western part. The dimmings look patchy, strongly different from an isotropic geometry often observed (cf., Chertok and Grechnev, 2003). The deepest depression of the EUV emission in dimming regions is about four times. Note also that there are loops visible in the last three frames of the two right columns that connect both active regions.

2.4. Polarization measurements from RATAN-600 data

Measuring magnetic fields from radio data has been extensively discussed in the literature (e.g., Kundu, 1965; Gelfreikh, 1972, 1994; Kundu and Alissandrakis, 1984; Gelfreikh, Pilyeva, and Ryabov 1997). The essence of the method is based on the fact that radio emissions generated in the presence of a magnetic field are circularly polarized, and the sense and the degree of polarization both depend on the particular emission mechanism as well as the magnetic field strength and direction in regions where the emission is generated and propagated. Hence, when the emission mechanism is identified, the degree of polarization of the radio emission provides an important constraint for the magnetic field strength.

A promising instrument for measuring magnetic fields in the corona is RATAN-600 due to two major advantages: 1) wide spectral range of 1–17 GHz with a high spectral resolution, and 2) huge effective area of the antenna which provides a very high sensitivity not reachable in observations with NoRH or SSRT. However, the technique of polarization measurements with RATAN-600 is rather complicated due to 1) properties of the complex antenna and feed systems, 2) properties of the complex multichannel spectrum analyzer and irregularities of its characteristics, 3) one-dimensional observation mode which produces data not as straightforward as two-dimensional images. All these apply to both total intensity and polarization measurements from RATAN-600 data. This is why we should make an emphasis on the accuracy of those measurements.

On November 23, 2000, solar observations at the RATAN-600 were carried out in the meridian (09:00 UT) and two azimuths (07:52 and 10:08). Right and left circularly polarized components (RCP and LCP) were recorded in 35 channels simultaneously within the wavelength range of 1.8–30 cm. A panoramic spectrum analyzer developed in SAO RAS (Bogod *et al.,* 1993) was used in the observations. The total intensity (Stokes *I*) and the circularly polarized component (Stokes *V*) are calculated as $I = RCP + LCP$ and $V = RCP - LCP$. The beam width (FWHM) is $17'' \times 13'$ at $\lambda = 2.0$ cm.

Due to sufficiently high spatial resolution of the radio telescope in the high-frequency domain of the operating frequency range, the radio source identified with the post-eruptive arcade is well separated from adjacent radio sources present in the solar scans at higher frequencies. For this reason, we analyze this radio source in detail in the range 1.8 – 4.95 cm only.

We estimate the flux density of the source from the ratio of its area in the scan to the total area under the entire scan. We use for the calibration of scans 1) observations of the Sun during solar minima, 2) observations of a reference radio source (Crab Nebula), 3) solar total flux measured with Nobeyama Radio Polarimeters as well as other total flux radiometers.

We take into account in the calibration routines the vertical cross section of the RATAN beam pattern at various wavelengths and the displacement of the source with respect to the beam center. The flux density of the source measured using different calibration methods differ within 20%.

We estimate the degree of polarization as a ratio of values measured from Stokes *V* and *I* scans. Because the profiles of the source in question in total intensity and polarization almost coincide, we calculate the degree of polarization as a ratio of either fluxes or maximum antenna temperatures of *V* and *I* images of the source. Here, the degree of polarization does not depend on the calibration method. The major error in the measurements of the degree of polarization is due to the isolation of the source from the record.

The degree of polarization measured for the source identified with the post-eruptive arcade is

$$r_c = (6.5 \pm 0.2)\% \quad \text{at}\ \lambda = 1.83\,\text{cm}, \quad \text{and}$$

$$r_c = (18 \pm 1)\% \quad \text{at}\ \lambda = 4.95\,\text{cm}.$$

In seven intermediate channels of this band, the degree of polarization is proportional to the wavelength within the measurement accuracy as expected for optically thin free-free emission. We do not consider the band of 2.67–3.21 cm, because the instrumental distortions in these channels are too high to be compensated.

To confirm the results of our measurements, we compare the characteristics estimated for the post-eruptive arcade with other radio sources observed on that day. One of them is identified with a large, single, leader sunspot of the 9236 group located close to the solar disk center, and another one is its diffuse following part without strong magnetic fields. We measured their characteristics using the same techniques. The spectrum of the leader sunspot sharply grows with wavelength, and the spectrum of the following part is actually flat within the analyzed frequency range. The degree of polarization for the sunspot-associated radio source is 90–75% in the 1.8–2.3 cm range, and then it decreases to 35–25% in the 4–5 cm range. The sunspot has a strong magnetic field at the photosphere (2400–2600 G), and the measured characteristics correspond well to the gyroresonance emission mechanism expected for this source. Similar parameters characterize a radio source associated with a leader sunspot of another group 9240 located close to the east limb that day.

The microwave characteristics of the post-eruptive arcade imply optically thin thermal bremsstrahlung as a predominant microwave emission mechanism. However, to estimate the magnetic field strength, one should make sure that the nonthermal contribution is negligible. Otherwise, the magnetic field strength can be well overestimated. We specifically address this issue in the next Section.

3. Discussion

3.1. Eruptive phenomena

3.1.1. *Filament Eruption*

Having disappeared between 05:12 and 05:47, the filament does not reappear during several subsequent hours, which confirms its disappearance because of ejection rather than due to a temporary temperature increase. Coincidence of all mentioned activity manifestations in both time and space within the interval of 05:36 – 05:40 over the whole observation data set in various spectral ranges provides evidence for their interconnection and relation to the filament ejection, flare, and CME subsequently recorded. The pre-eruptive brightening propagation during 04:09 – 04:58 visible in both Hα and EUV images from the southeast part of the sunspot group 9231 along its axis northwestward, to the filament, indicates a perturbation propagating in this direction. Then the perturbation reaches the filament, propagates counter-clockwise along it, and likely breaks its equilibrium. The complexity of the trajectory makes estimating the velocity of the perturbation difficult, because, as the Hα movie shows, the disturbance moves not only along the dominant direction, but also across it, i.e., along individual loops. It is also difficult to estimate Alfvén velocity in the region occupied by the filament, because the magnetic field in this region is not detectable in the SOHO/MDI magnetogram (that is, the magnetic field strength at the photosphere under the filament beyond the active regions does not exceed 30 G). Plasma density is also ambiguous. However, a rough estimation shows that the propagation time of the perturbation up to the southeast end of the filament is in accord with the event onset time. In summary, the observation data suggest that the trigger of the filament ejection (and the flare in AR 9238 as well as the CME) is the propagation of the perturbation caused by the flare at 04:09 – 04:58 in the southwest part of AR 9231. In turn, a probable trigger of the latter flare could be magnetic flux emergence in AR 9231 (cf., Heyvaerts, Priest, and Rust, 1977; Kundu and Shevgaonkar, 1985; Hanaoka, 1997; Hanaoka *et al.*, 1999; Kundu *et al.*, 2001).

The filament ejection is roughly simultaneous with the onset of the flare in AR 9238. The gap in Hα data rules out the possibility to establish which one of these two events occurred earlier, or that they really happened simultaneously. The microwave time profile of the flare of 05:36 – 06:15 at 17 GHz is predominantly thermal, and this is similar to a thermal post-eruptive burst analyzed by Uralov *et al.* (2002).

3.1.2. *Flare Geometry in Different Emissions*

Radio sources 4 – 7 are within the region where the filament existed prior to the eruption, i.e., above the magnetic polarity separation line. The sources are likely associated with tops of loops. Those regions are brightest in EUV; hence, they have the maximum density. In particular, the brightest source 6 corresponds to the brightest, densest region.

It was noted previously (e.g., Bastian, 1999; Grechnev and Nakajima, 2002) that, unlike extended Hα ribbons, flaring microwave sources are usually compact and do not exhibit two-ribbon configurations. However, in flares where the microwave emission is predominantly thermal like that one discussed by Uralov *et al.* (2002) as well as the flare under consideration, predominantly thermal sources are observed without conspicuous nonthermal processes that could visually surpass the thermal ones due to their high brightness. Therefore, the overall configurations of the active sources in the two flares observed in Hα, EUV, soft X-rays, and microwaves resemble each other. Note that due to the filament eruption, we can really deal in this Hα flare with appearance of some bright knots due to falling down remnants of the filament (Hyder, 1967), in addition to well-established reasons (particle precipitation and the density growth of the emitting plasmas in footpoints of flare and post-flare loops). In contrast, sufficiently dense plasmas in the coronal loops are responsible for their emission at 195 Å (as hot as 1.5 MK) and in soft X-rays (>2.5 MK). This can account for the differences in the configurations observed.

3.1.3. *Thermal Nature of the Microwave Emission*

The spectral characteristics of the post-eruptive arcade observed with the RATAN-600 correspond to thermal bremsstrahlung of the optically thin plasma (Borovik *et al.*, 2002a). This can be expected, because even the most powerful burst among the series of 05:36–06:12 is predominantly thermal. Adopting this emission mechanism with a temperature T $\sim$ 4 MK and total emission measure EM, from the well-known expression $S_{[\mathrm{sfu}]} \approx 3 \times 10^{-45}\,\mathrm{EM}_{[\mathrm{cm}-3]} T_{[\mathrm{K}]}^{-1/2}$ and using the technique by Akhmedov *et al.* (1987), we infer a plasma number density of (2–3) $\times 10^9\ \mathrm{cm}^{-3}$ at the time of the observations with the RATAN-600. Because the radio source is identified with the arcade observed in soft X-rays, we estimate the temperature from soft X-ray GOES data. The estimates of the emission measure obtained from radio and soft X-ray data are also in reasonable agreement.

3.1.4. *Polarization of the Microwave Flare Emission*

The considerations of the flux density as well as the fact that the ratios of the degree of polarization at 5.7 GHz (7–8%) and 17 GHz ($\sim$2.5%) are equal to the ratio of the wavelengths expected for optically thin free-free emission confirm the identification of the emission mechanism, virtually up to the flare time. Together with the identification of the radio source with the post-eruptive arcade, these imply that the polarization of the emission is due to the coronal magnetic field at the site where the radio emission is generated. Therefore, the variations of the polarization in the course of the flare are associated with the motion of the radio source across regions of somewhat different magnetic field strength and direction. Zero polarization at the onset of the flare is probably due to the locus of the unresolved radio source being at that time near tops of the magnetic loops where the line-of-sight component of the magnetic field is close to zero. The higher degree of polarization at 17 GHz before the event (5–7%) as well as close values measured with the RATAN-600 after the event suggest an essential contribution of the radio emission from the southwestern legs of loops, i.e., lower altitudes in the corona, corresponding to stronger magnetic fields and smaller viewing angles.

The magnetic field strength at the northeastern legs of loops is significantly weaker, and the microwave source is displaced from those legs southwestward. This is why the polarization of the microwave emission in that region is not detectable.

3.2. MAGNETIC FIELD

3.2.1. *Dominant Emission Mechanism in Microwaves*

The microwave emission of the post-eruptive arcade is dominated by optically thin free-free emission, because even at the flare peak the observed microwave flux density is close to the flux density computed from soft X-ray GOES data (see Figure 5). Hence, we estimate the magnetic field strength in the arcade assuming thermal bremsstrahlung to be the dominant emission mechanism, and this estimate will actually be the upper limit. However, some minor contribution of nonthermal emission, which can be strongly polarized, could increase the observed polarization, and some corrections should be applied to the estimate obtained. Therefore, our next step will be an estimation of the polarization contributed by nonthermal emission. We will take here the estimated magnetic field strength as the first approximation. The result will be also the upper limit for this nonthermal contribution.

First, we compare the total intensity of microwaves with soft X-ray emission. The brightness of the optically thin thermal free-free radio emission is proportional to the column emission measure and has a dependence on temperature $T^{-1/2}$. Soft X-ray emission is due to emission lines and thermal bremsstrahlung of optically thin hot plasmas ($T > 2.5$ MK) and has another temperature dependence. Long enough after the event, thermalization is completed and, assuming plasma within the arcade is nearly isothermal, we can expect the brightness of the thermal bremsstrahlung in microwaves to be proportional to the soft X-ray emission. Therefore, we expect a similarity of the optically thin thermal free-free microwaves and soft X-ray images. However, if gyromagnetic radio emissions are present, they would show up as compact bright radio sources in regions where the circular polarization is conspicuous. The gyromagnetic radio sources in total intensity would not have counterparts in soft X-rays, which are insensitive to the magnetic field.

Figure 9 shows how the radio source observed with the RATAN-600 is related to the post-eruptive arcade observed in soft X-rays with *Yohkoh*/SXT. We plot one-dimensional Stokes *I* and *V* scans observed with the RATAN-600 on top

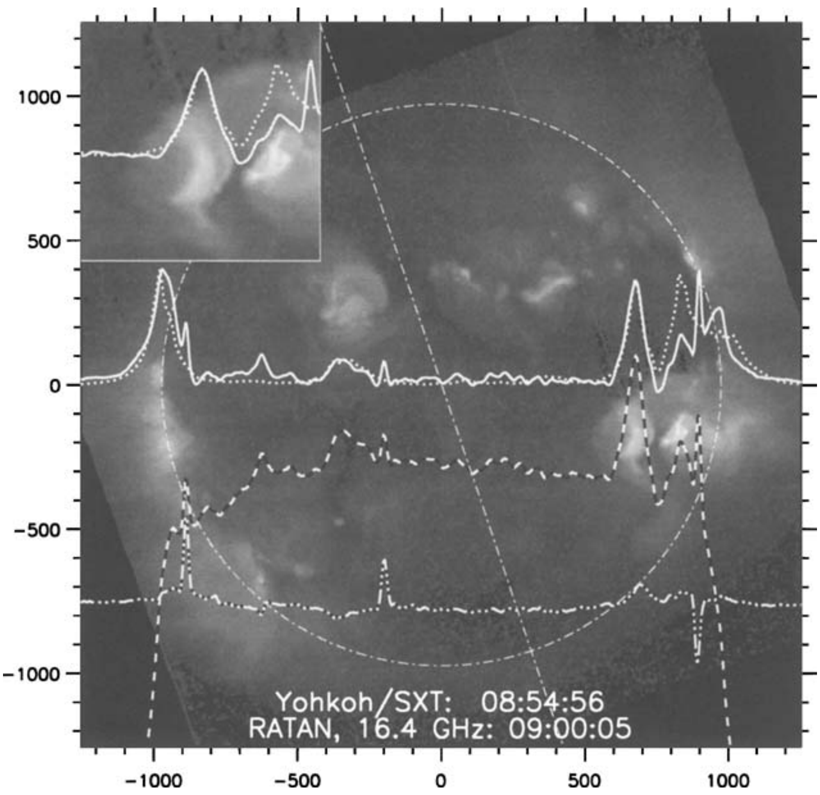

Figure 9. *Yohkoh*/SXT images overlaid with one-dimensional RATAN scans, Stokes *I* (*black*/*white dashes*), and Stokes *V* (*dash-three dots*) multiplied by 3 and shifted to show it better. *Solid line* shows Stokes *I* scan with subtracted quiet-Sun's level. *Dotted line* shows a model scan computed from the SXT image. Inclined *dash-dotted line* shows the polar axis of the Sun. Axes show arc seconds from the solar disk center. The inset shows the enlarged arcade region (center of [675″, −125″]).

of the *Yohkoh*/SXT image shown as a grayscale background. Because soft X-ray emission does not contain a contribution from the quiet solar disk, we have subtracted it from the total intensity scan. However, this procedure is not perfect in the one-dimensional case, especially close to the limb. We also plot in Figure 9 the model scan computed from soft X-ray data. This one-dimensional representation is convenient for the comparison, and it shows some quantitative features (see also Borovik *et al*., 2002b; Grechnev *et al*., 2003).

We see from Figure 9 that the microwave intensity and soft X-ray one-dimensional scans mostly resemble each other. Gyromagnetic peaks show up in both Stokes *I* and *V* scans in those regions where the microwave and soft X-ray scans do not match each other. The arcade region shows good correspondence of soft X-ray and microwave scans, and some minor discrepancies could be due to temperature variations, etc. This suggests that the microwave-emitting source is mainly hot plasma confined in the arcade observed in soft X-rays, and this also suggests that the estimate of the degree of circular polarization for thermal free-free emission applies to the data under consideration.

3.2.2. *Magnetic Field Strength Estimated from the Microwave Polarization*
Microwave thermal free–free emission from a homogeneous, thermal, optically thin, hot plasma within large-scale, weak coronal magnetic field B is circularly polarized in the sense of the x-mode with a degree $r_c \approx 2\cos\theta(\nu_B/\nu)$, where the gyrofrequency is $\nu_B = 2.8 \times 10^6 B$, and θ is the viewing angle relative to the direction of the magnetic field (Zheleznyakov, 1970; Dulk, 1985). A generalized expression for estimates of the magnetic field strength $B_{[G]}$ from the percentage of the polarization p at the wavelength of $\lambda_{[cm]}$ for free-free emission valid not only for the optically thin limit was proposed by Gelfreikh (1972, 1994): $B_{\parallel} = 107p/(n\lambda)$ with n being the power-law index of the brightness temperature spectrum. If the optical depth is small, both formulas give the same result.

In our case, the optically thin limit applies to the measurements, because the optical depth

$$\tau_{\mathrm{free-free}} = 0.0113\, n_0^2 L \nu^{-2} T^{-3/2} (\Lambda + \ln T - \ln \nu)$$

is small even at $\lambda = 10\,\mathrm{cm}$: $\tau_{(\lambda=10)} = 0.026$. This allows us to estimate the magnetic field strength from the RATAN-600 data on the polarization, and we obtain an estimate of the line-of-sight component of the magnetic field strength $B_{\parallel} \approx 190\,G$.

3.2.3. *Contribution from Nonthermal Gyrosynchrotron Emission*
On the other hand, contribution of gyrosynchrotron emission from power-law electrons could significantly increase the degree of polarization. To obtain the upper limit of the polarization due to nonthermal emission, we will take the estimated magnetic field of $B = 200\,\mathrm{G}$ up to 300 G (to account for the viewing angle) and the strongest parameters of the accelerated electrons appropriate to the event under consideration. In solar flares with pronounced nonthermal emissions, the fraction of accelerated electrons n_e/n_0 is typically 10^{-5}–10^{-4}, and their power-law index δ is usually from 6 for soft electron spectra up to 3 for hard electron spectra. We do not expect the nonthermal contribution to be large, because even at the flare peak it is not pronounced (see Figure 5). Hence, we assume that n_e/n_0 hardly exceeds 10^{-4}, and the power-law index δ is definitely steeper than 4. Taking the depth of the emitting volume $L \approx (1.5\text{–}2) \times 10^9$ cm and ambient plasma number density $n_0 \approx (2\text{–}3) \cdot 10^9 \mathrm{cm}^{-3}$, using formulas from Dulk (1985), with $B = 200$–$300\,\mathrm{G}$, we estimate the turnover frequency of the gyrosynchrotron emission $\nu_{\mathrm{peak}} \approx (1.5\text{–}2)\,\mathrm{GHz}$. Therefore, the gyrosynchrotron emission above 2 GHz must monotonically decrease with frequency. Taking an optically thin approximation, we estimate that if the fraction of the gyrosynchrotron emission at $\lambda = 10$ cm does not exceed 20% according to RATAN total flux measurements, then the addition of the polarization due to nonthermal component at

$\lambda = 1.8$ cm must not exceed $r_{c(\lambda=1.8)} < 0.2 \times (10/1.8)^{1.22-0.9\delta} \times r_{c\,gyro} < 0.3\%$ even with $r_{c\,gyro} \sim 1$, which is negligible. Hence, even if there is some contribution of nonthermal emission, it could not significantly change the estimate of the magnetic field strength in this case.

3.2.4. *Magnetic Field Strength Estimated from the Potential Field Extrapolation*

In addition, we extrapolated the magnetic field into the corona in the potential approximation (Rudenko, Altyntsev, and Lubyshev, 1998) using a part of the SOHO/MDI magnetogram of November 23, 06:24:02. The line-of-sight magnetic field component in the polarized microwave source is 710 G at the photosphere, and 195 G, 134 G, and 99 G at heights of 10, 15, and 20 thousand km, respectively, and the absolute value of the magnetic vector is, correspondingly, 1400 G, 341 G, 218 G, and 150 G. This confirms the estimate of the magnetic field strength from radio data and specifies the height of the radio source of $\sim$10 000 km.

Note that the optical depth of thermal bremsstrahlung $\tau_{\text{free-free}} \sim \nu^{-2}$ and a possible contribution of nonthermal emission (above the turnover frequency) both go down with frequency. Due to this circumstance, the polarization measurements for estimates of the magnetic fields from free-free emission should be performed at the highest frequency available. In this way, we also avoid possible contribution of gyroresonance emission.

3.3. Summary on the Event

Models of initiation and scenarios of eruptive events and related phenomena basically converge to interactions of either local, or large-scale, or global magnetic fields in various magnetic configurations (see the review by Klimchuk, 2002; Uralov *et al.*, 2002, and references therein). In the simplest case, the scenario of an eruptive event associated with a CME suggests a prominence/filament eruption observed at high altitudes as a structure component of the CME. An arcade is formed at the site of the pre-existing prominence/filament. The process of the arcade formation often proceeds energetically, through powerful thermal and nonthermal processes manifesting themselves as a post-eruptive flare. Dimmings observed at the site of the eruption and its surroundings have an anisotropic configuration which is typical of the period of the solar maximum unlike dish-like dimmings observed during the minimum of the solar cycle. The presence of dimmings in the surroundings of the site of the eruption indicates evacuation of material from a more extended region. So almost all of the mentioned phenomena are observed in the eruptive event under consideration.

The event was triggered by a flux emergence occurring in AR 9231. Its direct outcome was a series of subflares and flare-like disturbances in AR 9231 propagating toward the southwestern end of the filament. When the disturbance reached the filament, it was activated and ultimately erupted, which, in turn, triggered the flare in AR 9238. Note that the flux emergence that eventually caused the eruption in AR 9238 occurred far from the eruption site, in AR 9231. The chain of events discussed shows that the prime cause of an eruption, a flux emergence, may take place at a remote site, but, of course, in a region magnetically connected with the region of the eruption.

Note that the speed (and mass) of the CME is moderate, 500 – 600 km s^{-1}, with a low importance of the flare (C5.4). This indicates that the bulk of the stored energy which has released in the reformation of the magnetic configuration has been spent in the acceleration of the CME, and its minor part was released as the flare emissions. This confirms that particular conditions, including the energy storage and its form, essentially determine, which eruptive phenomena are pronounced to greater or lesser extent in a particular event (Maksimov, 2002).

4. Results and Conclusions

1. We have studied solar activity manifestations in various emissions on November 23, 2000, and found them to be connected with an eruptive event that occurred in the southwest quadrant of the solar disk, which included a filament eruption, Hα flare, and radio bursts, followed by a post-eruptive arcade formation at the eruption site, appearance of dimmings nearby, and a CME subsequently observed.
   - The eruptive event occurred in an activity complex consisting of active regions 9231 and 9238. It included almost all eruptive and post-eruptive phenomena, which allowed us to follow a chain of those events.
   - The whole story of the events was as follows: emergence of new magnetic flux resulted in a flare in AR 9231 which triggered activation and eruption of the filament followed by the CME and the flare in AR 9238 in which the post-eruptive arcade was observed.
   - The flux emergence that eventually caused the eruption in AR 9238 occurred far from the eruption site, in AR 9231. So, the prime cause of an eruption may take place at a remote site (but in a region magnetically connected with the region of the eruption).
   - The structure of predominantly thermal microwave flaring sources corresponds to the structures observed in Hα, soft X-ray, and EUV ranges in contrast to impulsive nonthermal flares, where microwave flaring sources are compact.
2. Using microwave data, we have studied the magnetic field in the post-eruptive arcade.
   - The polarized radio emission observed in the event visualizes regions of different magnetic field strength and direction. Motion of a polarized radio source allows studying the magnetic field distribution in an arcade. The

magnetic field strength was estimated to be $\sim$200 G at about 10 000 km in the corona. This estimate follows from radio data as well as extrapolation of the photospheric magnetic field into the corona.

– A special methodical issue is the importance of the microwave emission mechanism identification from observations in a wide spectral range. Improper interpretation of the polarization measurements can result in a well overestimated magnetic field strength in the corona. We have addressed a technique to estimate contribution of nonthermal emissions to the polarization observed. Polarization measurements for estimates of the magnetic fields from free–free emission should be performed at the highest frequency available.

Acknowledgements

We are grateful to M.A. Livshits for fruitful discussion, and to V.I. Garaimov for the assistance in processing RATAN-600 data. We are indebted to the unknown referee for useful, important remarks, which helped us to improve the paper. We thank the instrumental teams of the Nobeyama Radioheliograph, SSRT, and RATAN-600 radio telescopes; *Yohkoh*, SOHO, and GOES satellites for the open-data policies which made available for us data used in this study. We also used Hα images from Yunnan Observatory available in the Big Bear ftp archive. This work was supported by the Russian Foundation of Basic Research (02-02-16548, 03-02-16591, 03-02-17528, 03-02-17357), the Ministry of Education and Science (NSh 477.2003.2), Presidium of RAS (7/2004), 16 KI, and OFN 18.

References

Akhmedov, S. B., Bogod, V. M., Borovik, V. N., Willson, R., Gelfreikh, G. B., Dikiy, V. N., Korzhavin, A.N., Lang, K., and Petrov, Z. E.: 1987, *Bull. Spec. Astrophys. Obs.* **25**, 105 (in Russian).

Bastian, T. S.: 1999, in T. Bastian, N. Gopalswamy and K. Shibasaki (eds), Proceedings of the Nobeyama Symposium, Kiyosato, Japan, NRO Report No. 479, 211.

Bogod, V. M., Abramov-Maksimov, V. E., Dikiy, V. N., Vatrushin, S. M., and Tsvetkov, S. V.: 1993, Preprint SAO RAS No. 84, St. Petersburg, Russia (in Russian).

Borovik, V. N., Gelfreikh, G. B., Medar, V. G., and Grigorieva, I. Y.: 2002a, in Proceedings of 10th European Solar Physics Meeting, Prague, September 9–14 2002 (ESA SP-506), p. 431.

Borovik, V. N., Grechnev, V. V., Gelfreikh, G. B., Grigorieva, I. Y., and Medar, V. G.: 2002b, in Proceedings Conference on Active Processes on the Sun and Stars (in Russian), p. 148.

Chertok, I. M. and Grechnev, V. V.: 2003, *Astron. Rep.* **47**, 2, 139.

Dulk, G. A.: 1985, *ARA&A*, **23**, 169.

Gelfreikh, G. B.: 1972, in *Astronomicheskii Tsirkuliar* No. 699, p. 3 (in Russian).

Gelfreikh, G. B.: 1994, in V. Rušin, P. Heinzel, and J.-C. Vial, (eds), *Solar Coronal Structures*, *IAU Coll.* 144, (Slovakia: VEDA), p. 21.

Gelfreikh, G. B., Pilyeva, N. A., and Ryabov B. I.: 1997, *Solar Phys.* **170**, 253.

Gosling, J. T.: 1993, *J. Geophys. Res.* **98**, 18937.
Grechnev, V. V.: 2003, *Solar Phys.* **213**, 103.
Grechnev, V. V. and Nakajima, H.: 2002, *Astrophys. J.* **566**, 539.
Grechnev, V. V., Lesovoi, S. V., Smolkov, G. Ya., Krissinel, B. B., Zandanov, V. G., Altyntsev, A. T., Kardapolova, N. N., Sergeev, R. Y., Uralov, A. M., Maksimov, V. P., and Lubyshev, B. I.: 2003, *Solar Phys.* **216**, 239.
Hanaoka, Y.: 1997, *Solar Phys.* **173**, 319.
Hanaoka, Y., Sakurai, T., Sato, J., and Gopalswamy, N.: 1999, in *Yohkoh* 8th Anniversary Symposium on Explosive Phenomena in Solar and Space Plasma, The Institute of Astronautical and Space Science, p. 99.
Heyvaerts, J., Priest, E. R., and Rust, D. M.: 1977, *Astrophys. J.* **216**, 123.
Hyder, C. L.: 1967, *Solar Phys.* **2**, 267.
Kundu, M. R.: 1965, *Solar Radio Astronomy*, Interscience Publication, New York.
Kundu, M. R. and Alissandrakis, C. E.: 1984, *Solar Phys.* **94**, 249.
Kundu, M. R. and Shevgaonkar, R. K.: 1985, *Astrophys. J.* **297**, 644.
Kundu, M. R., Grechnev, V. V., Garaimov, V. I., and White, S. M.: 2001, *Astrophys. J.* **563**, 389.
Maksimov, V. P.: 2002, *Solar-Terr. Phys.* **2**, 13.
Rudenko, G. V., Altyntsev, A. T., and Lubyshev, B. I.: 1998, in A. Antalová and A. Kučera (eds), *JOSO Annual Report* 1997, Tatranská Lomnica, Slovak Republic, p. 94.
Uralov, A. M., Lesovoi, S. V., Zandanov, V. G., and Grechnev, V. V.: 2002, *Solar Phys.* **208**, 69.
Zheleznyakov, V.: 1970, *Radio Emission of the Sun and Planets*, Pergamon, Oxford.